

Winds from massive stars: implications for the afterglows of γ -ray bursts

Enrico Ramirez-Ruiz,¹[★] Lynnette M. Dray,¹ Piero Madau^{1,2} and Christopher A. Tout¹

¹*Institute of Astronomy, Madingley Road, Cambridge, CB3 0HA*

²*Department of Astronomy and Astrophysics, University of California, Santa Cruz, CA 95064, USA*

Accepted 2001 June 16. Received 2001 April 30; in original form 2000 December 18

ABSTRACT

Recent observations suggest that long-duration γ -ray bursts (GRBs) and their afterglows are produced by highly relativistic jets emitted in core-collapse explosions. The pre-explosive ambient medium provides a natural test for the most likely progenitors of GRBs. Those stars that shed their envelopes most readily have short jet crossing times and are more likely to produce a GRB. We construct a simple computational scheme to explore the expected contribution of the presupernova ejecta of single Wolf–Rayet (WR) stars to the circumstellar environment. Using detailed stellar tracks for the evolution of massive stars, we discuss the effects that the initial main-sequence mass, metallicity, rotation and membership in a binary system have on the ambient medium. We extend the theory of GRB afterglows in winds to consider the effect of the relativistic fireball propagating through the WR ejecta. Specific predictions are made for the interaction of the relativistic blast wave with the density bumps that arise when the progenitor star rapidly loses a large fraction of its initial mass or when the ejected wind interacts with the external medium and decelerates. A re-brightening of the afterglow with a spectrum redder than the typical synchrotron spectrum (as seen in GRB 970508, GRB 980326 and GRB 000911) is predicted. We also calculate the luminosity of the reflected echo that arises when circumstellar material Compton-scatters the prompt radiation, and examine the spectral signatures expected from the interaction of the GRB afterglow with the ejected medium.

Key words: supernovae: general – gamma-rays: bursts – X-rays: bursts.

1 INTRODUCTION

Recent evidence has given support to the idea that long-duration γ -ray bursts (GRBs) result from the cataclysmic collapse of massive stars in very energetic supernova-like explosions (MacFadyen, Woosley & Heger 2001) rather than the coalescence of two compact objects, such as black holes or neutron stars (Lattimer & Schramm 1976). The observed distribution of optical afterglow luminosities with respect to their host galaxies suggests that some GRBs may be associated with star-forming regions (Paczynski 1998). The spatial and temporal coincidence between the supernova (SN) 1998bw and GRB 980425 (Galama et al. 1998) hints that some GRBs may be linked to ultra-bright type-Ibc SNe, but this is still controversial (Pian et al. 2000). Some evidence for supernova-type emission has also been found in GRB 980326 (Bloom et al. 1999), GRB 970228 (Reichart 1999) and GRB 000911 (Lazzati et al. 2001). If we believe that GRBs are associated with SN-like events, then the explosion is likely to be jet-induced if the baryon contamination problem is to be avoided (Rees & Mészáros 1992). Without collimation, the maximum

isotropic γ -ray emission is raised to unprecedented values, implying a total energy of the order of 3×10^{54} erg (GRB 990123; Kulkarni et al. 1999). A beamed jet alleviates this energy requirement. The evidence is still preliminary, but collimation factors of $\Omega_j/4\pi < 0.01$ have been derived from the decline in some afterglow light curves (Kulkarni et al. 1999; Castro-Tirado et al. 1999; Harrison et al. 1999). Whether a jet is present or not, the energy budget is compatible with current scenarios that involve the collapse of compact objects: the binding energy of the orbiting debris and the spin energy of the black hole are the two main energy reservoirs available (Rees 1999).

MacFadyen & Woosley (1999; hereinafter MW99) have explored the evolution of rotating helium stars whose iron core collapse does not produce a successful traditional neutrino-powered explosion. For massive stars ($M_0 \gtrsim 35 M_\odot$) with sufficient angular momentum, a rapidly accreting stellar mass black hole forms promptly at the centre of the collapsing star (Type I collapsars). Less rapidly accreting black holes can also form over longer time-scales owing to the infall of stellar material that failed to escape during the initial SN (Type II collapsars). Prompt and delayed black hole formation can occur in stars with a range of radii depending on the evolutionary state of the massive progenitor,

[★]E-mail: enrico@ast.cam.ac.uk

its metallicity and its membership in a binary system. If the star loses its hydrogen envelope along the way, and if the jet produced by the accretion maintains its energy for longer than it takes the jet to tunnel through the star, a GRB is likely to be produced (MW99). Otherwise, acceleration of the explosion debris to a sufficiently high Lorentz factor ($>10^2$, Mészáros & Rees 1997) is unlikely and an asymmetric supernovae like SN 1998bw may result (MacFadyen et al. 2001).

In the collapsar model for GRBs, or in any other model involving a massive star, the key to obtaining relativistic motion is the escape of an energy-loaded fireball from the stellar environment. This is aided if the progenitor undergoes a Wolf–Rayet (WR) phase, which is characterized by a strong stellar wind that causes the star to lose enough of its outer layers for the surface hydrogen abundance to become minimal. The radius of a WR star is sufficiently small for the explosion energy to break out before the engine ceases to operate. Because of the intrinsic variations of mass-loss rates in WR evolution, the GRB blast wave expands into shells of varying gas density. The effects of the WR ejecta interacting with the interstellar medium (ISM) can be observed in the wind bubbles around some of these objects. The deceleration of a pre-SN wind by the pressure of the surrounding medium or the interaction of fast and slow winds (Luo & McCray 1991; Vikram & Balick 1998) could also create circumstellar shells.

It is an unavoidable consequence of a core collapse model for GRBs that the afterglow emission propagates in a dense stellar wind. Chevalier & Li (1999, 2000) described some features of the afterglow evolution in a steady, spherically symmetric wind with density $\propto r^{-2}$. In this paper we study the effects of strong, non-steady WR stellar winds with large mass-loss variations and non-spherical geometries. In particular we explore the impact of the pre-SN evolution of single high-mass stars¹ ($M_0 \gtrsim 35 M_\odot$) on the circumstellar environment. In Section 2 we use detailed stellar evolution of WR stars to show how the progenitor initial mass (M_0) and metallicity Z affect the density profile of the ambient material. In Section 3 we extend the theory of afterglows in winds to consider the propagation of a relativistic fireball through the dense environment expected at the end of the evolution of a WR star. We calculate the echo that arises when the progenitor circumstellar material Compton-scatters the prompt γ -ray radiation in Section 4. Implications of recent observations, in particular for GRB 970508, GRB 980326 and GRB 000911, and predictions for future ones, are discussed in Section 5. We examine the spectral line signatures expected from the interaction of a GRB afterglow with the chemically enriched environment in Section 6. Our conclusions are presented in Section 7.

2 EVOLUTIONARY MODELS OF MASSIVE STARS WITH HIGH MASS-LOSS RATES

2.1 Model outline

2.1.1 WR evolution

WR stars have many extreme properties: they have luminosities typically between 10^5 and $10^6 L_\odot$ and are very hot. This places them in the upper left corner of the HR diagram. Because of their dense stellar winds ($10^{-4} M_\odot \text{yr}^{-1}$), the hydrostatic surfaces of WR stars are mostly inaccessible to direct observations. This makes it difficult to associate stellar models with observed objects

on the basis of their radii, surface temperatures or luminosities. The spectroscopic determination of the abundances of H, He, C, N and O (e.g. Smith & Hummer 1998) allows only certain classes of theoretical stellar models. Massive stars are known to have stellar winds and mass loss while on the main sequence and, although the amount of mass lost here may be small compared with that lost in later phases, it is relevant to the subsequent evolution. The first evolutionary phase of a WR star is the nitrogen-line stage (WNL), which begins when CNO-processed material is exposed at the stellar surface. This progresses to the WNE stage, during which no surface hydrogen is detectable. Once the hydrogen envelope is completely lost, the WR models strictly obey the mass–luminosity relationship for hydrogenless WR stars. This allows the details of their further evolution to be calculated by solving only the equation of global energy conservation (Langer 1989) for a given mass-loss rate, because the mass determines the luminosity, which in turn determines the rate of nuclear burning in the stellar core. After the helium envelope is shed, the WC stage occurs, in which strong carbon lines can be seen. Finally, WO stars are formed, with high surface oxygen abundances. Subclassifications in the above categories are made according to line strength ratios (e.g. Smith & Maeder 1991).

In order to assess the simplest case, we shall confine the discussion in this section to non-rotating, non-magnetic single stars. We use detailed evolutionary tracks between the initial main sequence and the WO stage, with enhanced mass-loss rates based on the work of Meynet et al. (1994). We carry out computational simulations with the stellar evolution code first developed by Eggleton (1971) and recently updated by Pols et al. (1995). Owing to slight differences in the stellar evolution codes, including a different treatment of convective overshooting (Schröder et al. 1997), the stellar tracks computed by Meynet et al. (1994) are not identical with those calculated here (e.g. the minimum initial mass for WR star formation is slightly lower) but they are qualitatively the same.

As described in Meynet et al. (1994), enhanced mass-loss rates were used during the phases when stellar winds are believed to be driven by radiation pressure, i.e. during the whole evolution with the exception of the WNE and WC/WO phases, which correspond to the stage of nearly pure helium envelopes and of He + C + O cores, respectively. Enormous mass loss can occur at the entrance into these stages. Pre-WR mass-loss rates for the whole HR diagram were taken from the expression derived by de Jager et al. (1988) and scaled with metallicity as $(M_z/M_\odot) = (Z/Z_\odot)^{0.5}$. For WNL stars, a constant mass-loss rate was adopted (Abbott & Conti 1987) and for later stages of WR evolution a mass-dependent mass-loss rate was assumed as specified by Langer (1989). In cases where the cumulative WNL mass loss was enough nearly to evaporate the star, we used the WNE rate instead.

2.1.2 Wind–ISM interaction

Winds from the most massive stars tend to have the greatest effect on the ISM because the mass-loss rates are large and the winds are very fast and carry large momentum fluxes. Moreover, massive stars tend to lie in associations, so there is the cumulative influence of the winds of many stars. In describing the effects of stellar winds on the surrounding medium we used the basic theory for the wind–ISM interaction developed by Castor, McCray & Weaver (1975). We assume that the ISM has a simple structure, with no clumps, no magnetic fields, no multiple ionization phases and no nearby stars. During the evolution of a wind-driven circumstellar shell, the

¹ The comparative modelling of single and binary systems will be presented in a subsequent paper (Dray et al., in preparation).

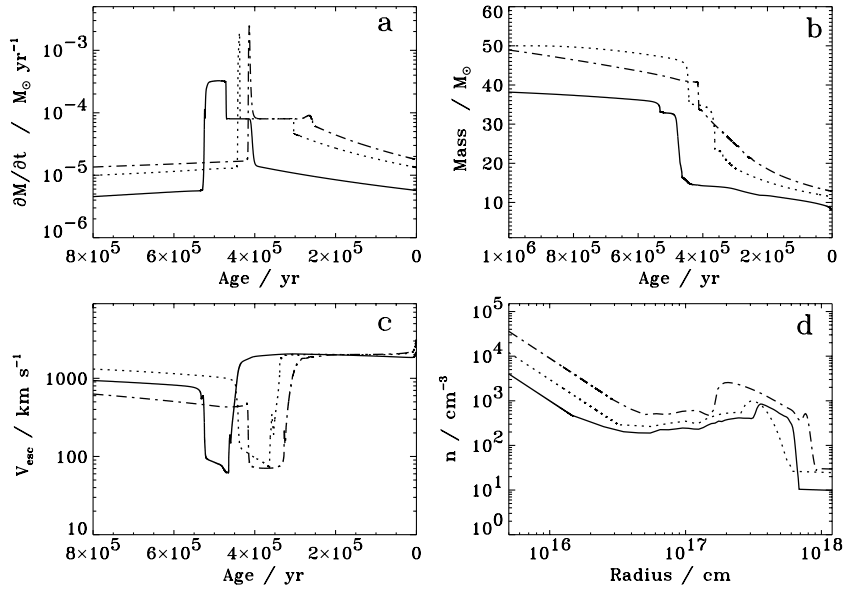


Figure 1. Stellar winds from different evolutionary WR models. The state of the ambient medium of a WR star at the end of its life (d) is determined primarily by the time evolution (until core collapse) of the mass-loss rate (a) and the escape velocity of the wind (c). Panel (b) shows the mass of the WR star as a function of time. Stellar models were computed for initial masses of 40 (solid line), 50 (dotted line) and 60 (dash–dotted line) M_\odot . The external medium particle density of the wind ejected by the progenitor is best modelled (at $r \leq r_{\text{dec}}$, see equation 1) by a power-law $n = Ar^{-2}$. A spherical shell with high column density arises when the ejected material accumulates at the radius at which the free expansion phase of the ejected wind terminates. We have set the density of the ambient material before the WR phase to 1 cm^{-3} .

system has a four-zone structure (analogous to that of a supernova shell; Cox 1972; Woltjer 1972). From the inside, to the outside these zones are: (I) a supersonic stellar wind with density $\rho(r) = \dot{M}/4\pi r^2 v_\infty$; (II) a hot, almost isobaric region consisting of shocked stellar wind mixed with a small fraction of the swept-up interstellar gas; (III) a thin, dense, cold shell containing most of the swept-up interstellar gas; (IV) ambient interstellar gas of number density n_0 .

The wind initially expands unopposed into the ISM with a velocity of about v_∞ , the escape velocity at the sonic point (for the purpose of this analysis we assume $v_\infty = (2GM_*/R_*)^{1/2}$, because the sonic point is reached after a few stellar radii). The free expansion phase is considered to be terminated at a time t_{dec} , when the swept-up mass of the interstellar medium is comparable with the mass in the wind (Woltjer 1972; Castor et al. 1975; McCray 1983). The mass lost by the star is $\dot{M}t_{\text{dec}}$ and the swept-up mass is $(4\pi/3)(v_\infty t_{\text{dec}})^3 n_0 m_p \mu_c$, where $\mu_c \sim 2$ in a helium gas. These two masses are equal when $t_{\text{dec}} = [3\dot{M}/(4\pi v_\infty^3 n_0 m_p \mu_c)]^{1/2}$, which is about 100 yr for a typical WR wind expanding into an homogeneous ISM.² During this time the wind bubble has reached a radius of

$$r_{\text{dec}} = 8.8 \times 10^{17} \dot{M}_{-5}^{1/2} n_{0,0}^{1/2} v_{\infty,3}^{-1/2} \text{ cm}, \quad (1)$$

where \dot{M} is the mass-loss rate in units of solar masses per year, n_0 is the density of the surrounding medium in units of cm^{-3} , v_∞ the wind velocity in units of km s^{-1} and we adopt the convention $Q = 10^x Q_x$.

In a dense ($n_0 \approx 10^5 \text{ cm}^{-3}$) molecular cloud, a wind-driven bubble will radiate its energy and stall in a short time, causing the ejected wind to slow rapidly at a much smaller radius (Shull 1982). The same may be true if a neighbouring star is present – for

example, a very close binary in which the WR wind is strongly slowed down by the OB star radiation pressure before it collides with the OB wind. $R_{\text{OB}} < r_{\text{OB}} \leq r_{\text{ter}}$, where r_{OB} is the distance from the OB star (with radius R_{OB}) to the region of the stellar wind collision and $r_{\text{ter}} \approx 5R_{\text{OB}}$ is the distance from the OB star centre at which the OB wind reaches terminal velocity.³ Many WR stars with absorption lines appear to be single; however, the fraction of visible close WR + OB binaries seems to be around 35 per cent (Chiosi & Maeder 1986).

When the free expansion phase (I) has ended, the wind encounters an inward facing shock. Kinetic energy is deposited in the shocked wind region in the form of heat,

$$T_{\text{shock}} = \frac{3}{16} \frac{m_p \mu_c}{k} (\Delta v)^2 = 1.4 \times 10^5 \left(\frac{\Delta v}{100 \text{ km s}^{-1}} \right)^2 \text{ K}, \quad (2)$$

where Δv is the relative speed of the material approaching the shock. This creates a temperature of about 10^7 K in the shocked wind region. During phase II, the material is so hot that it causes the contact surface to move outward more slowly than it would in a freely expanding wind. The ISM that enters the outward facing shock is heated to a temperature below 10^6 K , emission of line radiation becomes the dominant cooling process and the swept-up gas cools quickly to temperatures of about 10^4 K that can be maintained by the radiation field of the star. The duration of the adiabatic expansion phase can thus be estimated by finding the time it takes the expanding gas to cool from 10^7 to 10^6 K . Using equation (2), we find that a change in temperature from 10^7 to 10^6 K corresponds to a change in jump velocity by a factor of $\sqrt{10}$. This change in jump velocity represents a phase II:phase I age ratio

² The free expansion phase takes place at the early stages of the evolution of the hot star and occupies a minimal fraction of its lifetime. During this time both \dot{M} and v_∞ are approximately constant (see Figs 1a and 1c).

³ If a very close binary is present, the high-density region will probably be reduced to a small covering factor surrounding the collapsing star. Note that a beamed fireball would introduce an additional geometrical factor.

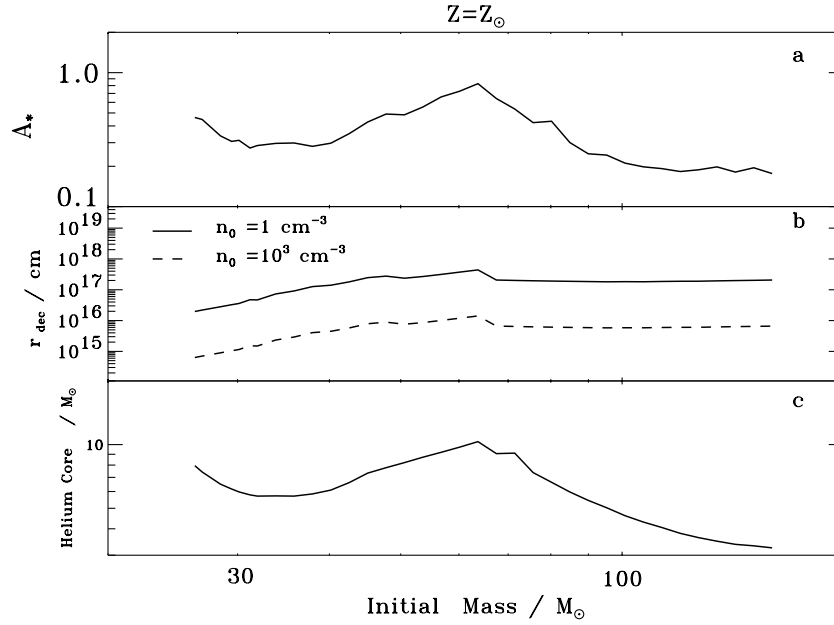


Figure 2. The effects of different initial masses on the structure of the ambient medium. The density profile can be fitted by a power law $n(r) = Ar^{-2}$ for $r < r_{\text{dec}}$. The value of the constant A as a function of M_0 is shown in panel (a) for the stellar models computed in Section 2.1. A was scaled to $A = 3.0 \times 10^{35} A_* \text{ cm}^{-1}$. The radial location of the highest density shell as a function of M_0 is shown in panel (b) for different values of n_0 . The free expansion of the ejected wind is terminated when the swept-up mass becomes comparable with the mass of the wind. The ejected mass then accumulates at such a radius (r_{dec}). This overdense region lies closer to the progenitor for WR stars originating from low-initial-mass stars. All the evolved WR stars have lost their hydrogen envelope and are left with a bare helium core – see panel (c).

of about 6 (McCray 1983). Thus, the age of the adiabatic phase is less than about 1000 yr.

The mass of the swept-up material is much larger than that in the hot wind and, because it is cool, it lies in a compressed region. Phase III persists for as long as the star is able to sustain a powerful wind. The dominant energy loss of region II is work against the compressed region III (see Castor et al. 1975). The compressed region III expands because its gas pressure is higher than that of the surrounding ISM. Therefore, the expansion is described by the momentum equation

$$\frac{d}{dt}[M_S(t)v(t)] = 4\pi r^2(t)P_i, \quad (3)$$

where P_i is the internal pressure of the compressed region, assuming that most of the swept-up interstellar mass remains in the thin shell. $M_S(t)$ is the mass of the shell of swept-up material, given by $M_S(t) = (4/3)\pi r^3(t)\rho_0$. P_i is determined by the gas pressure of the high-temperature gas in region II. The wind material that enters the backward facing shock is hot, but the material that enters the forward facing shock is cool. The cooled swept-up material is driven outward by the high gas pressure of the hot bubble. The stellar wind adds energy to region II at a rate $L_w(t) = \frac{1}{2}\dot{M}(t)v_\infty^2(t)$. The internal energy in the bubble is given by the product of the energy per unit mass of the material, $(3/2)nkT/\rho_i = (3/2)P_i/\rho_i$, and the total mass of the bubble, $(4/3)\pi r^3\rho_i$. Since the total internal energy of the bubble comes from the energy of the wind, we find $\dot{P}_i = L_w(t)/[2\pi r^3(t)]$ (Castor et al. 1975; McCray 1983). The expansion of the bubble during the adiabatic phase can be found numerically by using this expression in the momentum equation.⁴

⁴ If the wind power L_w is roughly constant for a period of time t , one can write $P_i = L_w t / (2\pi r^3)$. The resulting solution of equation (3) gives $r(t) \propto t^{3/5}$. This shows that the shell expands more slowly than would a freely expanding wind.

The bubble could continue to expand until stalled by the pressure of the ISM. However, before that happens, the star will have produced a supernova type explosion, which re-pressurizes the bubble.

2.1.3 Wind–wind interaction

During the different mass-loss stages within a WR lifetime, the wind power of the star increases or decreases with time (as shown in Fig. 1a). When the escape velocity of the wind increases, the fast wind collides with the early ejecta before reaching r_{dec} . The resultant shell will be pushed outward by the central star wind and retarded by the early ejected wind, quickly reaching a constant velocity, but increasing in mass. The basic theory of the wind–wind interaction was developed by Kwok, Purton & Fitzgerald (1978). The resulting expansion law for the shell follows from the momentum balance between the two components (denoted as i and j). If M_{ij} is the mass of the resulting shell when it is at a radial distance $r_{ij}(t)$, then

$$M_{ij}(t) = \int_{r_j+v_j t}^{r_{ij}(t)} \frac{\dot{M}_j}{v_j} dr + \int_{r_{ij}(t)}^{r_i+v_i t} \frac{\dot{M}_i}{v_i} dr, \quad (4)$$

where $v_j < v_i$. If $v_{ij}(t)$ is the velocity of the shell, then, assuming a completely inelastic collision, the equation of motion may be written

$$M_{ij}(t) \frac{dv_{ij}}{dt} = \frac{\dot{M}_i}{v_i} [v_i - v_{ij}]^2 - \frac{\dot{M}_j}{v_j} [v_j - v_{ij}]^2. \quad (5)$$

Numerical integration of equation (5), with a substitution for $M_{ij}(t)$ from equation (4), gives the resulting expansion law for the shell. The thickness of the shell Δr_{ij} may be found by requiring its

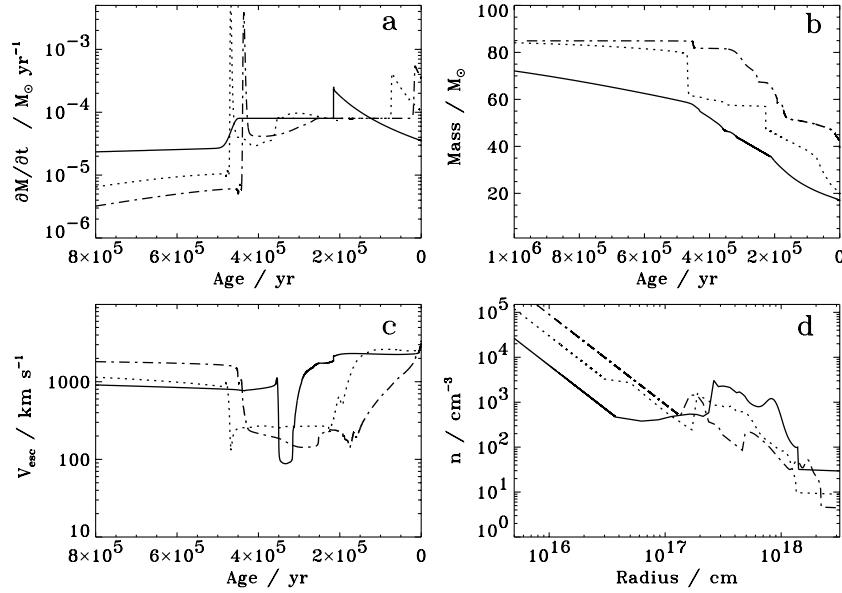


Figure 3. The effect of metallicity on stellar winds. An $85\text{-}M_{\odot}$ main-sequence star was evolved with three different metallicities: $Z = 0.5 Z_{\odot}$ (solid line), $Z = 0.05 Z_{\odot}$ (dotted line), $Z = 0.015 Z_{\odot}$ (dash-dotted line). Low metallicity decreases the mass-loss rate (a), increases the mass of the helium core (b) and keeps the radius of the star small, reducing the escape velocity of the stellar wind (c). Also, low metallicity favours high mass-loss rates at the end of the WR phase, increasing the density of the ambient medium (d) at $r \leq r_{\text{dec}}$. A spherical shell with high column density arises when the ejected wind interacts with the ISM ($n_0 = 1 \text{ cm}^{-3}$) and decelerates. In the case of the $85\text{-}M_{\odot}$ main-sequence star with $Z = 0.015 Z_{\odot}$, a thin shell is present at $r \leq r_{\text{dec}}$ owing to the substantial change in mass-loss prior to core collapse.

internal pressure to balance the pressure from the wind (see Kwok et al. 1978).

2.2 The effects of mass loss during the evolution of WR stars

An increase of the mass-loss rate has profound consequences for the modelling of the WR population. At a given metallicity, the minimum initial mass for the formation of a WR star (lower for higher \dot{M}), the duration of the WR stage (greater for higher \dot{M}), the times spent in the different WR subtypes and the surface composition during these phases are all very sensitive to the mass-loss rates. A detailed discussion is given in Maeder (1991). Here we emphasize some interesting contributions to the structure of the ambient medium that arise when the ejected winds interact with the ISM during the WR lifetime (about 10^5 yr).

Using the physical ingredients mentioned in Section 2.1, we have computed the evolution of stars with initial main-sequence masses M_0 between 10 and $150 M_{\odot}$ and of solar metallicity $Z_{\odot} = 0.02$. Fig. 1a shows the time evolution (until core collapse) of the mass-loss rate for $M_0 = 40, 50$ and $60 M_{\odot}$. The progenitor star loses a large fraction of its initial mass quite rapidly on entering the WNL phase (the highest constant mass-loss rate interval in Fig. 1a). The main reason is the non-negligible contribution of the H-burning shell to the total luminosity. Depending somewhat on the steepness of the hydrogen profile above the H-burning shell, the WNL stage is rather short in low-initial-mass stars; its duration increases towards higher masses and it may last for the whole post-main-sequence phase for the highest masses (Langer 1987). Owing to the existence of a H-burning shell and also because hydrogen has a high radiative opacity and a low mean molecular weight, the radii of WNL stars are considerably larger (and their surface temperatures correspondingly smaller) than WNE and WC stars. The escape velocity of the wind therefore decreases during this phase, as shown in Fig. 1c. During the early

phase of WR evolution, the progenitor stars lose a large fraction of their initial mass quite rapidly, as shown in Fig. 1b. We have studied the interaction of the strong stellar winds with the surrounding interstellar gas and have found that a dense circumstellar shell develops at the radius at which the free expansion phase of the ejected wind terminates, as illustrated in Fig. 1d. For a given metallicity, this overdense region is more extensive for higher initial masses.

In most early discussions (Chevalier & Li 1999; Madau, Blandford & Rees 2000; Mészáros, Rees & Wijers 1998; Panaitescu & Kumar 2000), the progenitor star was expected to be surrounded by a substantial

$$n(r) = Ar^{-s} \quad (6)$$

medium at the end of its life (with $s = 2$ for a wind ejected at a constant speed). For the stellar models computed here, we found no significant deviations from an r^{-2} density gradient as a result of the small mass-loss variations from the progenitor star prior to core collapse. We calculated power-law indices s with values ranging from 1.9 to 2.1. By running stellar models with a variety of initial masses, we found that the constant A in the density profile is not a strong function of M_0 , as shown in Fig. 2a. The constant A in equation (6) was scaled to $A = 3.0 \times 10^{35} A_{*} \text{ cm}^{-1}$ as in Chevalier & Li (2000). The highest deviation from the extrapolated density profile is mainly provoked by the interaction between the winds and the interstellar medium. As time progresses, the amount of material swept up increases and the momentum from the wind cannot drive the shell to such high speeds. The ejected mass then accumulates at a corresponding radius, creating an overdense region. We found the radial location of the overdense region (or ‘bump’) to be smaller for WR stars that originate from low-initial-mass stars (see Fig. 2b). The radius at which the free expansion ends is a function of the product $\dot{M}^{1/2} v_{\infty}^{-1/2} n_0^{-1/2}$, so that one may fear that large variations of n_0 can be masked or mimicked by much

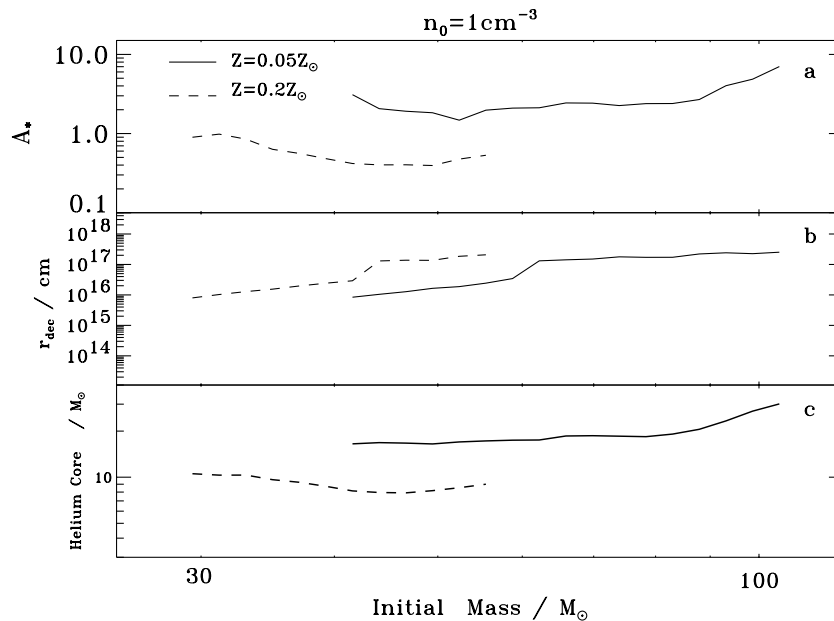


Figure 4. Stellar winds from WR models with different metallicity. All the evolved WR stars have lost their hydrogen envelope. The value of the normalization constant A_* as a function of M_0 is shown in panel (a) for different values of Z . The highest density shell lies closer to the progenitor for WR stars originating from lower Z (see panel b). Low metallicity raises the threshold for removal of the hydrogen envelope by stellar winds, increasing the mass of the helium core (panel c).

smaller variations of M_0 (or $\dot{M}^{1/2} v_\infty^{-1/2}$; see Fig. 2b). It should be remarked that the plausible range of n_0 ($0.1\text{--}10^5\text{ cm}^{-3}$) is large compared with the plausible range of M_0 ($M_0 \geq 35 M_\odot$ if GRBs originate from rapidly rotating massive stars with large helium cores, Fig. 2c).

2.3 The role of metallicity

Metallicity Z influences the stellar evolution of massive stars mainly through bound–free and line opacities. The main source of opacity in the interior is electron scattering, which is independent of metallicity. Therefore, metallicity has little direct structural effect in massive stars. Bound–free and line opacities, on the other hand, are important in the outer layers of massive stars. In this way, metallicity influences the mass-loss rates by stellar winds (Chiosi & Maeder 1986). Low metallicity keeps the radius of the star smaller and also reduces the mass loss. Both effects inhibit the loss of angular momentum from the evolving star (MW99). For a given mass-loss rate, the lower the metallicity, the higher the stellar mass for WR formation. Furthermore, low metallicity raises the threshold for the removal of the hydrogen envelope by stellar winds, thus increasing the mass of the heaviest helium core and favouring black hole formation (MW99).

We have computed the evolution of stellar models for an initial main-sequence mass of $85 M_\odot$ at three different metallicities: $Z = 0.5 Z_\odot$, $Z = 0.05 Z_\odot$ and $Z = 0.015 Z_\odot$ (see Fig. 3). As discussed above, low metallicity reduces the mass loss for most of the WR lifetime. However, low metallicity favours high mass-loss rates at the end of WR evolution (see Fig. 3a). This increases the density of the ambient medium at small radii prior to core collapse (see Fig. 3d). Nevertheless, the overall amount of ejected material that accumulates at r_{dec} increases with metallicity, as shown in Fig. 3d.

By running stellar models with a variety of main-sequence initial masses and metallicities, we found that the normalization constant

of the density profile, A_* , is not a strong function of Z , as shown in Fig. 4a. The highest deviation from the extrapolated profile occurs at progressively smaller radii for WR stars originating in low-metallicity environments (see Fig. 4b). In such environments, the formation of massive helium stars, desired for GRB formation, is favoured (see Fig. 4c).

The numbers of WR stars in galaxies of different metallicities are an important test of the stellar models at various Z and of the values of the final stellar masses. The theoretical predictions of the ratios of WR/O-stars, WC/WR and WC/WN are in very good agreement with observations of the Local Group (Maeder 1991). This supports the adopted dependence of the mass-loss rates on metallicity (Meynet et al. 1994). At high Z (in inner galactic locations), gas opacities are larger in the outer stellar layers and so more momentum is transferred by radiation pressure, mass loss is more intense and thus GRB formation is disfavoured. The strong dependence of massive star evolution on metallicity suggests that GRB progenitors in inner galactic locations may be intrinsically different from those in outer ones. Furthermore, this dependence on Z implies that GRB characteristics could be strongly affected by redshift (MW99).

2.4 The effects of WR rotation

If long GRBs are SN-like events, the explosion is likely to be the outcome of black hole formation through the collapse of a rapidly rotating massive star (WM99; Heger, Langer & Woosley 2000). Rotation may affect WR evolution in several ways (Maeder & Meynet 2000, and references therein). First, in the case of fast rotation, the star may enter the WR phase while still burning hydrogen in its core and thus spend more time there. Second, rotation (through its effects on both the mass-loss rates and mixing) may favour the formation of WR stars with lower initial mass. Typically, the minimum mass for WR formation is $35\text{--}40 M_\odot$ for non-rotating models. It decreases to about $25 M_\odot$ for initial

$V_{\text{rot}} = 300 \text{ km s}^{-1}$ (Maeder & Meynet 1987). Finally, higher rotation-velocities lead to longer WR lifetimes and higher mass-loss rates. Thus, rotation could alleviate the need to enhance the mass-loss rates in order to reproduce the observed WR/O-star number ratio as originally proposed by Meynet et al. (1994).

Direct attempts to measure the rotation velocity of WR stars have been performed only for a few cases: Massey (1980) obtained $v \sin i \sim 500 \text{ km s}^{-1}$ for WR138 (see also Koenigsberger 1990); Massey & Conti (1981) measured $v \sin i \sim 150\text{--}200 \text{ km s}^{-1}$ for WR3. Also, indirect evidence has been found for the existence of some axisymmetric features around WR stars. For example, Harries et al. (1998) suggest that about 15 per cent of WR stars have anisotropic winds caused by equatorial density enhancements produced by rapid rotation. High rotation velocities for iron cores favour the collapsar model for GRBs (see MW99). The contribution of the WR mass loss to the surrounding medium along the GRB beam, which is likely to be close to the rotation axis of the star, may be smaller than calculated here for the spherical wind case.

3 WIND INTERACTION MODELS FOR GRB AFTERGLOWS

One can understand the dynamics of the afterglows of GRBs in a fairly simple manner, independent of any uncertainties about the progenitor systems, from the relativistic generalization of the method used to describe supernova remnants. The basic model for GRB afterglow hydrodynamics is a relativistic blast wave expanding into the surrounding medium (Mészáros & Rees 1997). The interaction of the outer shell with the external medium is described by the adiabatic self-similar solution due to Blandford & McKee (1976, hereafter BM). The scaling laws that are appropriate for the burst interaction with a medium with particle density $n \propto r^{-s}$ have been described by Mészáros et al. (1998), Chevalier & Li (1999, 2000) and Panaitescu & Kumar (2000). We aim to examine the specific predictions for the interaction of the relativistic blast wave with the density bumps that arise when ejected stellar material decelerates against the external medium (see Section 2). This collision would be an important contribution to the observed afterglow if it were not that it takes place too late in the fireball evolution. We outline the relevant physical parameters that determine when this collision occurs in Section 3.1. We discuss briefly the situation when the burst is collimated in Section 3.2. We analyse the shock conditions when the shell collides with an enhanced density medium in Section 3.3, and estimate the synchrotron emission that results and its observational consequences in Section 3.4.

3.1 Hydrodynamics of a relativistic shell

For an adiabatic ultra-relativistic blast wave, the (isotropic equivalent) total energy is

$$E = \frac{8\pi A \Gamma^2 r^{3-s} c^2}{17-4s}, \quad (7)$$

where Γ is the bulk Lorentz factor of the shock front and r is the observed radius near the line of sight (BM). We assume the burst to be collimated with an initial half-angle θ larger than 20° , and that lateral expansion is negligible during the relativistic phase. A distant observer receives a photon emitted along the line of sight towards the fireball centre at a time $t = r/4(4-s)\Gamma^2 c$ (Chevalier

& Li 2000), and so

$$r = \left[\frac{(4-s)(17-4s)Et}{2\pi A c} \right]^{1/(4-s)}. \quad (8)$$

Before the collision with the high-density shell, the shock front is expected to propagate through an $n(r) = Ar^{-s}$ wind. In a spherically symmetric wind ejected at a constant speed the density drops as $s = 2$. Using the stellar models in Section 2, we found $0.1 < A_* < 10$ for WR stars surrounded by an $s \approx 2$ medium at the end of their life ($A_* = A/3.0 \times 10^{35} \text{ cm}^{-1}$). For these stellar parameters, a re-brightening of the afterglow as a consequence of the collision of the shock front with the high-density spherical shell is observed at a time

$$t_{\text{day}} \approx 0.25 \left(\frac{E}{10^{52} \text{ erg}} \right)^{-1} \left(\frac{r_{\text{shell}}}{10^{17} \text{ cm}} \right)^2 A_* \quad (9)$$

after the burst. Here t_{day} is the observer time measured in days. If the collision takes place at a sufficiently late phase of the afterglow the system is adiabatic. This is probably valid from about half an hour after the burst (Granot, Piran & Sari 1998). The outer shell catches up with the thin high-density shell, which is at rest at a radius r_{shell} . The shell collision produces two new shock waves: a forward shock that moves into the thin shell and a reverse shock that propagates into the relativistic ejecta. The calculation of shocks in the collision of two cold shells resembles the calculation of energy emitted from internal shocks (Kumar & Piran 2000).

3.2 Collimation of γ -ray bursts

The energy flux from a GRB may be collimated, as witnessed in the jets from active galactic nuclei and some binary black hole sources. Some models explicitly include this collimation (MW99). As long as the jet is highly relativistic, the observed features are reproduced by spherical models, but as the shocked jet slows down there are clear consequences for the observed afterglow (Rhoads 1997): the edge of the jet becomes visible when $\Gamma = (2\theta)^{-1}$ and the jet is able to expand laterally, leading to an exponential slowing of the forward shock front. In the case of a collimated GRB going off in a medium with density decreasing as r^{-2} , jet effects are expected to become important at a time $t_{\text{jet}} \approx 2(\theta/0.1)^4 E_{52} A_*^{-1} \text{ d}$ (Chevalier & Li 2000). Kumar & Panaitescu (2000) have recently pointed out, however, that a fireball propagating into an $s = 2$ medium should show little evidence for light-curve steepening due to edge and sideways expansion. This could explain the lack of breaks in the afterglow light curves of GRB 980326 and GRB 980519. In a collimated outflow the sharpest break in the light curve occurs in a uniform low-density medium and is associated with the edge of the jet approaching the relativistic beaming cone. In wind scenarios, where no clear break in the light curve is predicted, jets can perhaps be detected by time-dependent measurements of polarization (Kumar & Panaitescu 2000).

For a collimated outflow expanding in an r^{-s} medium, the observed radius near the line of sight is proportional to $(Et/\theta^2 Ac)^{1/(4-s)}$. Thus, for a fixed value of E , the impact of the relativistic shell with a density bump would take place earlier in the evolution of the fireball if the burst is collimated, causing a re-brightening of the afterglow to appear at earlier times in the observer's frame.

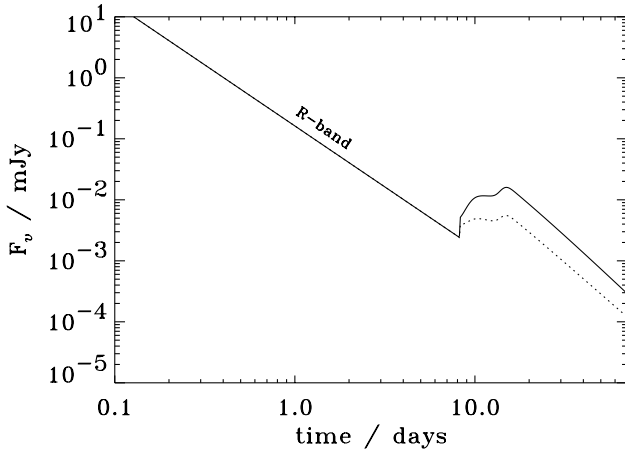


Figure 5. The effect of the impact of a relativistic shell with the density discontinuity on the optical afterglow. The shock front expands within the $s = 2$ stellar wind until it reaches the high-density shell at a distance $r_{\text{shell}} \approx 4 \times 10^{17}$ cm. The radial profile of the high-density shell is modelled as the inner bump shown in Fig. 1d for the $40\text{-}M_{\odot}$ case. Collisional models were computed for a high-density enhancement $\alpha = 100$ (solid line) and a low-density enhancement $\alpha = 10$ (dotted line). At the time of the collision, the relativistic shell Lorentz factor is $\Gamma \sim 3$ for $E_{52} = 0.5$, $A_* = 1$, $\varepsilon_e = 0.1$, $\varepsilon_B = 1.0$, and $p = 3$. The afterglow emission is calculated in the adiabatic regime. The collision model takes into account the fireball geometrical curvature when calculating the photon arrival time and relativistic boosting. Given the radius of collision $r_{\text{shell}} \gg l$, the observed variability time-scale is $\Delta t_{\text{obs}} \approx r_{\text{shell}}/(c\Gamma^2) > 20$ d. Note that $\Gamma \ll 3$ after the collision.

3.3 Shock conditions

Consider a relativistic shell with a Lorentz factor η moving into a cold external medium (EM). The interaction is described by two shocks: a forward shock propagating into the EM and a reverse shock propagating into the shell. There are four regions separated by the two shocks: the EM (1), the shocked EM (2), the shocked shell material (3) and the unshocked shell material (4). The EM is at rest relative to the observer. From the jump conditions for the shocks and the equalities of pressure and velocity along the contact discontinuity we can estimate the Lorentz factor γ , the number density n and the energy density e in the different shocked regions as functions of the three quantities n_1 , n_4 and η (BM). The unshocked EM has $\gamma_1 = 1$, while the unshocked shell material moves at the original coasting velocity of the particles, $\gamma_4 = \eta$. The afterglow emission is determined by the deceleration time of the shell. The emitting region moves toward the observer with a Lorentz factor $\Gamma = \gamma_2 = \gamma_3$, assuming that the shocked material (either region 2 or 3) emits radiation on a time-scale shorter than the hydrodynamical time.

There are two limits in which there is a simple analytical solution (Sari & Piran 1995). If the shell density is high, $n_4 \gg \eta^2 n_1$, then the reverse shock is Newtonian (or mildly relativistic). In this case the energy conversion takes place in the forward shock, and the collision is too weak to slow down the shell efficiently, $\Gamma \sim \eta$. If the density of the expanding shell is low, $n_4 \ll \eta^2 n_1$, then the reverse shock is relativistic, the shell material decelerates considerably and

$$\Gamma \sim (n_4/n_1)^{1/4} (\eta/2)^{1/2}. \quad (10)$$

The energy density in the shocked regions satisfies

$e = e_2 = e_3 = 4\Gamma^2 n_1 m_p c^2$. Similar relations hold for the reverse shock (Sari & Piran 1999). In any realistic situation the EM is probably inhomogeneous, as in the stellar models in Section 2.

Consider a density jump by a factor α over a distance l . The forward shock propagates into the EM with a density n_1 as before, and when it reaches the position where the EM density is αn_1 a new shock wave is reflected. This shock is reflected again off the shell. Sari & Piran (1995) showed that the reflection time is $\approx l/(4c\alpha^{1/2})$. After these reflections the Lorentz factor and hydrodynamical properties of the system are as if the EM were homogeneous with a density αn_1 . The corresponding observed time-scale due to this inhomogeneity of the EM is $t \approx l/(\alpha^{1/2}\Gamma)$ (for $l \gtrsim r$).

3.4 Synchrotron emission

The synchrotron spectrum from relativistic electrons that are continuously accelerated into a power-law energy distribution comprises four power-law segments, separated by three critical frequencies, the self-absorption frequency (ν_{sa}), the cooling frequency (ν_c) and the characteristic synchrotron frequency (ν_m) (Sari et al. 1998; Mészáros et al. 1998). The spectrum and light curve of an afterglow are determined by the time evolution of these frequencies, which in turn depend on the hydrodynamical evolution of the fireball.

The break frequencies can be calculated if the energy distribution of the injected electrons and the strength of the magnetic field are both known. The distribution of the injected electrons is assumed to be a power law of index $-p$, above a minimum Lorentz factor $\gamma_i \approx \varepsilon_e (m_p/m_e) \Gamma$. The energy carried by the electrons is a fraction $(p-1)/(p-2)$ of the total internal energy ε_e . The turbulently generated magnetic field, assumed to be amplified up to a fraction ε_B by the processes in the shocked region and not determined directly by the field in the WR star, is $B \approx \sqrt{32\pi c \varepsilon_B^{1/2} m_p^{1/2} n_1^{1/2}} \Gamma$ (Sari, Piran & Narayan 1996). For an adiabatic blast wave, the corresponding observer peak frequency is

$$\nu_m \propto \frac{B}{m_e c} \gamma_i^2 \Gamma. \quad (11)$$

The ratio of $\nu_{m,\alpha}$ the observed peak frequency from the relativistic shell after the forward shock has traversed a density jump of a factor α over a distance l , and the frequency in the absence of such a jump ν_m , is

$$\frac{\nu_{m,\alpha}}{\nu_m} \approx \frac{\Gamma_\alpha^4 (\alpha n_1)^{1/2}}{\Gamma^4 n_1^{1/2}} \approx \alpha^{-1/2}. \quad (12)$$

Therefore, we expect this emission to be a very significant contribution to the short-wavelength flux. The spectrum at low frequencies ($\nu \ll \nu_m$) scales as $\nu^{1/3}$; at high frequencies ($\nu \gg \nu_m$) it scales as $\nu^{-(p-1)/2}$. At late times, when the collision has run its course, the shells have merged back to a BM solution and the observed flux is proportional to $E_\alpha^{(p+1)/[2(4-s)]}$ for $n(r) \propto r^{-s}$. In the absence of a density enhancement, the flux would have been proportional to $E^{(p+1)/[2(4-s)]}$ (Kumar & Piran 2000). Therefore, the increase in the observed emission from the forward shock due to the density jump is approximately $(E_\alpha/E)^{(p+1)/[2(4-s)]} \approx \alpha^{(p+1)/[4(4-s)]}$, neglecting the enhanced energy losses from the shocks that may arise during the collision with the high-density thin shell. We should expect, however, a smooth transition from one solution to the other at most wavelengths. This is not the case at frequencies for which there is significant emission from the reverse shock, from which the

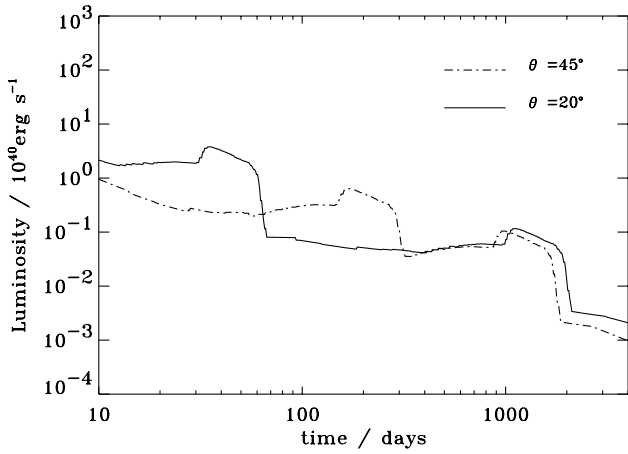


Figure 6. The Compton echo of a GRB. The primary burst is assumed to be a two-sided collimated pulse of energy $10^{52} \text{ erg s}^{-1}$ and duration 10 s, propagating at an angle θ to the line of sight, and invisible to the observer. The GRB jet propagates through the dense environment expected at the end of the evolution of a $40 M_{\odot}$ Wolf–Rayet star with Z_{\odot} (see Fig. 1d).

total emission is smaller, and at a lower frequency by typically a factor of Γ . At these frequencies the impact of this additional emission is likely to be significant.

We conclude that the impact of the relativistic shell with the density discontinuity (see Figs 1d and 3d) produces a bump in the light curve that can be very dramatic at low frequencies. To illustrate this, we consider the scaling laws described by Chevalier & Li (1999) for an adiabatic blast wave in an $s = 2$ medium. Before the collision, the synchrotron emission frequency of the lowest energy electrons is $\nu_m = 5 \times 10^{12} \epsilon_{e,-1}^2 \epsilon_{B,-1}^{1/2} E_{52}^{1/2} t_{\text{day}}^{-3/2} \text{ Hz}$ and the flux at this frequency is $F_{\nu_m} = 20 A_* \epsilon_{B,-1}^{1/2} E_{52}^{1/2} t_{\text{day}}^{-1/2} \text{ mJy}$ (these expressions assume $z = 1$ in a flat Universe with $H_0 = 65 \text{ km s}^{-1} \text{ Mpc}^{-1}$). For electrons with a power-law distribution p , the flux above ν_m is $F_{\nu} = F_{\nu_m} (\nu/\nu_m)^{-(p-1)/2} \propto t^{-(3p-1)/4}$. Over the typical time of observation of a GRB afterglow, the shock front expands within the stellar wind until it reaches the high-density bump at a distance of about $4 \times 10^{17} \text{ cm}$. The impact of the relativistic shell with the density enhancement produces a clear feature in the afterglow light curve. Fig. 5 shows the effect for two different values of the bump density. The light curve of the enhanced emission arising from the interaction of the forward shock with the density bump is calculated with the contribution of the curvature to the temporal structure described in Fenimore, Madras & Nayakshin (1996). Given a typical radius of collision $r_{\text{shell}} \gg l_{\text{shell}}$, the observed variability time-scale is $\Delta t_{\text{obs}} \approx r_{\text{shell}}/(\Gamma^2 c)$. The maximum enhancement of the observed emission with respect to the extrapolated afterglow light curve is approximately $\alpha^{1/2}$ and the characteristic synchrotron frequency is lower than that in the absence of the collision.

4 COMPTON ECHOES

If massive stars are the progenitors of GRBs, then the hard photon pulse will propagate in a pre-burst stellar wind. The GRB is assumed to have a broken power-law spectrum, $\epsilon E_{\epsilon} \propto \epsilon$ ($\epsilon \leq 250 \text{ keV}$) and $\epsilon^{-0.25}$ ($\epsilon > 250 \text{ keV}$). Circumstellar material Compton scatters the prompt radiation and gives rise to a reflection echo (Madau et al. 2000). If $E = \int E_{\epsilon} d\epsilon$ is the total energy

emitted by the burst, where $E_{\epsilon\Omega}$ is the energy emitted per unit energy ϵ and unit solid angle Ω along the θ direction, then the equivalent isotropic luminosity of the Compton echo inferred by a distant observer is

$$L_{\epsilon} = 4\pi \int n_e(r) E_{\epsilon\Omega} \frac{d\sigma}{d\Omega} \frac{dr}{dt} d\Omega, \quad (13)$$

where r is the distance from the site of the burst, $d\sigma/d\Omega$ is the differential Klein–Nishina cross section for unpolarized incident radiation, σ_T is the Thomson cross section, ϵ' is the energy of the scattered photon and n_e the local electron density. The equal-arrival time scattering material lies on the paraboloid determined by

$$r = \frac{ct}{1 - \cos \theta}, \quad (14)$$

where θ is the angle between the line of sight and the direction of the reflecting gas as seen by the burst.

Madau et al. (2000) derived analytical expressions for the echo luminosity light curve in the Thomson regime for a range of possible emission geometries and ambient gas distributions. In particular, they discussed the effect of an infinitesimal high-density spherical shell in the surrounding medium. For isotropic emission, the echo luminosity decreases as the equal-arrival time paraboloid sweeps up the shell, reaching a minimum when $t = r_{\text{shell}}/c$, and then increases until it reaches the back of the shell. For a collimated burst, the echo light curve is the sum of two delta functions, the result of the interaction of the approaching and receding jet with the spherical shell (see equation 10 in Madau et al. 2000). The two spikes of emission are seen separated by an interval $2r_{\text{shell}} \cos \theta/c$, where θ is the angle between the line of sight and the approaching beam (i.e. the main burst emission is not seen by the observer).

Fig. 6 shows the reflected echo of a two-sided GRB jet propagating through the dense environment expected at the end of the evolution of a $40 M_{\odot}$ Wolf–Rayet star with Z_{\odot} (see Fig. 1d). We calculated the luminosity of the reflected echo by integrating equation (13) with the full Klein–Nishina cross section. The GRB is assumed to radiate a total of 10^{53} erg , with each jet having equal strength. On the equal-arrival time paraboloid, the receding beam is reflected by denser gas that is closer to the source, and so its contribution dominates the echo at all energies where the scatter occurs in the Thomson regime. This is clearly illustrated by the second spike of the echo caused by the interaction of the receding jet with the density bump in the surrounding medium. The spectral energy distribution mirrors the prompt burst at low energies, but is much steeper above a few hundred keV (Madau et al. 2000). The hard X-ray flash from a pulse propagating into the environment expected at the end of the evolution of a $40 M_{\odot}$ star could be detectable by *Swift* out to $z \approx 0.1$.⁵ It is instructive to look at the contribution of the density bump to the luminosity of the reflected echo. The time interval between the two spikes, $2r_{\text{shell}} \cos \theta/c$, can be used to determine the angle between the line of sight and the approaching beam.

5 RECENT OBSERVATIONS AND FUTURE PREDICTIONS

5.1 Afterglow sources

The variety of observed afterglows, while compatible with relativistic fireball models (Mészáros et al. 1998), poses challenges

⁵ *Swift* is a NASA space mission planned for launch in 2003.

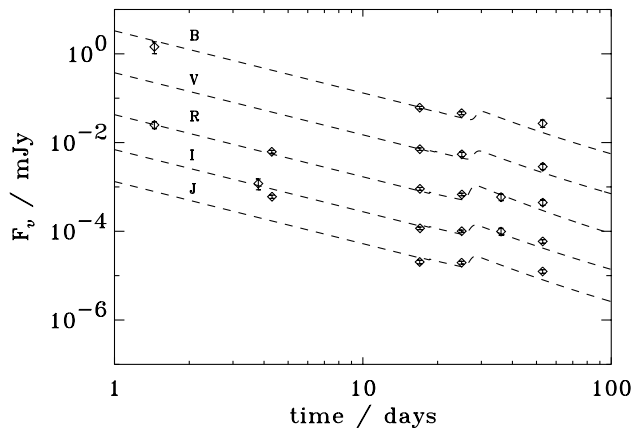


Figure 7. Modelling of the multi-filter light curves of the afterglow of GRB 000911. From top to bottom the normalized photometric measurements are plotted, scaled by factors of 10^2 , 10^1 , 1, 10^{-1} and 10^{-2} for clarity. The dashed lines show the best fit for a collisional model obtained by computing the interaction of a relativistic blast wave with the WR ejecta.

for interpretation. Some of the key questions include the effect of the external medium, the possible anisotropy of afterglow emission and the radiative efficiency. In this paper, we have considered the effects of the surrounding medium due to massive WR stellar progenitors on GRBs. We found that a high-density bump arises when the ejected wind interacts with the external medium and decelerates, or when the progenitor star rapidly loses a large fraction of its initial mass. The impact between the relativistic shell and this density bump could be observed as a re-brightening⁶ of the afterglow with a spectrum typically redder than the synchrotron afterglow spectrum, as seen in GRB 980326 and GRB 970228. These observations have been explained as an underlying supernova outshining the afterglow some days after the burst event. However, this interpretation should be regarded as tentative, in consideration of the fact that only *R*-band measurements and a low signal-to-noise spectrum were obtained for GRB 980326. In the case of GRB 970228 no spectroscopic measurement was made at the time of the suggested re-brightening, and the light curve was unevenly sampled in different filters.

5.1.1 GRB 970228 & GRB 980326

In order to explain the re-brightening of GRB 980326, we would require a large density jump with a size comparable with the variability time-scale, about 10Γ lightdays $\approx 10^{17}$ cm, and located at a distance $20\Gamma^2 c \text{ days} \approx 10^{18}$ cm (Bloom et al. 1999). These conditions are clearly compatible with the density jumps calculated in Section 2. A very red spectrum $F_\nu \propto \nu^{-2.8}$ (compared with $F_\nu \propto \nu^{-1.0}$ in the extrapolated afterglow) can be produced if there is some contribution to the emission from the reverse shock at lower frequencies. In the case of GRB 970228 at $z = 0.695$, the isotropic luminosity is $6 \times 10^{51} \text{ erg s}^{-1}$. The temporal bump detected 10 d after the explosion can be explained by the impact of a relativistic shell expanding within an $n(r) = A_* r^{-2}$ stellar wind with the density discontinuity located at a distance 5×10^{17} cm (see equation 9). These values are in agreement with the overdense regions calculated in Section 2.

⁶ Note that a re-brightening can also be produced by shock refreshment due to delayed energy injection by an extremely long-lived central engine. In this case, however, the spectrum would be bluer than a typical GRB afterglow (see Panaitescu, Mészáros & Rees 1998 for the case of GRB 970508).

5.1.2 GRB 000911

Using detailed stellar tracks for the evolution of massive stars, as described in Section 2, we found that the re-brightening of GRB 000911 at $z = 1.1$ (Lazzati et al. 2001), can be explained by the interaction of a relativistic blast wave ($\epsilon_e = 0.1$, $\epsilon_B = 0.1$ and $p = 2.2$) expanding into the ambient medium expected at the end of the life of a $40 M_\odot$ ($7 M_\odot$ core) WR star evolving with $Z = Z_\odot$. The shock front expands within an $n(r) = 1.5 \times 10^{35} \text{ cm}^{-1} r^{-2}$ stellar wind until it reaches the density enhancement (see Fig. 1d). The very red spectrum $F_\nu \propto \nu^{-5}$ (compared with $F_\nu \propto \nu^{-1.4}$ in the extrapolated afterglow) can be better reproduced if there is a substantial contribution to the emission from the reverse shock at lower frequencies. We have fitted this model to the simultaneous multi-filter data (see Fig. 7), obtaining a reduced χ^2 intermediate between the fit with a simple external shock synchrotron component plus a galaxy model ($\chi^2 \sim 1.3$) and the fit with the additional SN component ($\chi^2 \sim 1.1$, see Lazzati et al. 2001).

5.2 Internal shock models

In the internal shocks scenario for GRBs, the actual γ -ray temporal profile is the outcome of the complex dynamics of the ejecta. A growing consensus is that a central site releases energy in the form of a wind or multiple shells over a period of time commensurate with the observed duration of GRBs (Rees & Mészáros 1994). Each subpeak in the γ -ray light curve is the result of a separate explosive event at the central site. In this early phase, the time-scale of the burst and its overall structure follow, to a large extent, the temporal behaviour of the source. In contrast, the subsequent afterglow emerges from the shocked regions of the external medium where the relativistic flow is slowed down and the inner engine cannot be seen directly. A concern was raised that internal shocks without deceleration were rather inefficient (Kobayashi, Piran & Sari 1997), converting at most 25 per cent of the bulk motion energy into radiation. Since the afterglows can only account for a few per cent of the radiated energy, it is unclear where most of the energy goes.

In a dense molecular cloud, the density of the surrounding medium, before the free expansion phase, can be as large as $n_0 \approx 10^4$ – 10^5 cm^{-3} (Shull 1982; Sanders, Scoville & Solomon 1985). This is not unlikely because massive stars tend to cluster and these stars do not live long enough to travel far from their place of birth. In this environment the free expansion phase of the ejected wind, which is terminated when the swept-up mass becomes comparable with the mass in the wind, ends at a radius of 10^{15} – 10^{16} cm (see equation 1). The ejected mass then accumulates at such a radius, creating an overdense region. Substantial internal energy can be converted into radiation at this radius when the shells responsible for the γ -ray emission run into this region. This is equivalent to the model proposed by Fenimore & Ramirez-Ruiz (2001), with the dense region acting as the decelerating shell. No substantial deceleration is required to convert up to 80 per cent of the bulk-motion energy during the GRB. Indeed, a recent analysis of 387 pulses in 28 BATSE GRBs shows that the most intense pulses within a burst have nearly identical widths throughout the burst, but that the weak pulses tend to become wider as the burst progresses (Ramirez-Ruiz & Fenimore 2000). This effect is seen in internal shock simulations when a high-density thin shell at a radius of 10^{15} – 10^{16} cm is included. Furthermore, the detection of an optical flash associated with GRB 990123 (Akerlof et al. 1999), with a peak magnitude of 9 in the V-band 50 s after the initial burst

(successfully described by the reverse shock model in Sari & Piran 1999), can also be explained as a result of the impact of two shells that collide with a relative Lorentz factor of the order of 2 (Kumar & Piran 2000). Such collisions are expected in internal-shock models if an ejected shell catches up with a decelerating shell or when a shell runs into a dense region at a radius of 10^{15} – 10^{16} cm.

6 THE γ -RAY BURST ENVIRONMENT

The task of finding useful progenitor diagnostics is simplified if the pre-burst evolution leads to a significantly enhanced gas density in the immediate neighbourhood of the burst. The detection of spectral signatures associated with the GRB environment would provide important clues about the triggering mechanism and the progenitor. Stars interact with the surrounding interstellar medium, both through their ionizing radiation and through mass, momentum and energy transfer in their winds. Mass-loss leads to recycling of matter into the interstellar medium, often with chemical enrichment. Mass-loss is a particularly significant effect in the evolution of massive stars – in particular, for stars that enter WR stages. WR stars follow all or part of the sequence WNL, WNE, WC and WO, which corresponds to a progression in the exposure of nuclear products: CNO equilibrium with H present; CNO equilibrium without H; early visibility of the products of the 3α reaction; and then a growing (C + O)/He ratio, respectively. Mass-loss drastically influences stellar yields. At low Z there is a high production of α -nuclei, while at higher Z most of the He and C produced is ejected in stellar winds and escapes further nuclear processing.

The environment could also be metal-enriched, although solar abundances are probably more likely. The amount of metals in the environment can be larger than the stellar yields if a supernova explosion occurs before the GRB, perhaps producing significant Fe $K\alpha$ and K-edge luminosities (Lazzati, Campana & Ghisellini 1999). Because of the very high luminosities and hard initial γ -ray spectrum, all the Fe is fully ionized; as it cools, the strong Fe $K\alpha$ and K-edge appear initially in absorption, then later as recombination emission features (Weth et al. 2000). Guided by the report of Fe line detections that peak after 1 day in GRB 970508 and GRB 970828 (Piro et al. 1999; Yoshida et al. 1999), we are led to consider a high-density shell. A physical requirement is that the distance $ct\Gamma(t)^2$, reached after 1 day by the afterglow shock, is less than the shell radius. Notice that, in order to reproduce the observed Fe $K\alpha$ equivalent widths, a shell located at a few 10^{16} cm is required with a mass of Fe $\sim 2.5 \times 10^{-4} M_{\odot}$, in a total shell mass of $1 M_{\odot}$ (Weth et al. 2000). Such enhanced density shells can be present in the environment of a progenitor star if the density of the surrounding medium, before the WR phase, is of order 10^5 cm^{-3} . The ejected mass accumulates at this radius, creating a high-density region of 10^9 – 10^{11} cm^{-3} for a $50 M_{\odot}$ main-sequence star. Without substantial deceleration of the wind ejecta, such high-density shells are difficult to form. Emission lines are hard to detect, unless the event occurs in an exceptionally dense or metal-rich environment (Piro et al. 2000). A massive star environment could be distinguished by the presence of a significant flux of Fe $K\alpha$ and probably H Ly α emission lines, reprocessed by a moderately Thompson thick envelope. For a more massive thick envelope, a significant reflected component would be expected, in which Fe absorption edges and $K\alpha$ features would be present (Mészáros & Rees 1998; Amati et al. 2000).

7 CONCLUSIONS

Recent observations strongly suggest that at least some GRBs are related to massive supernovae. Quantitative insight into the formation of GRBs is hindered by the lack of detailed core-collapse calculations. The ground-breaking work of MW99 suggests that GRBs are more likely to occur in stars that have lost their hydrogen envelope. Stars with less radiative mass loss retain a hydrogen envelope in which a poorly collimated jet that loses its energy before breaking through the stellar surface is likely to arise. Highly relativistic jets will not escape red supergiants with radii $> 10^{13}$ cm. By contrast, a focused low-entropy jet that has broken free of its stellar cocoon is likely to arise from a WR progenitor. Our detailed stellar tracks for the evolution of a WR star show the diverse effects that initial main-sequence mass, metallicity and rotation can have on the surrounding medium. Pre-explosion mass loss provides a natural medium to generate GRB afterglows, and allows specific predictions about their temporal structure to be made. The presence of density bumps in the nearby ambient environment are inherent to the evolution of WR stars. The impact between the forward shock and these high-density regions should be observed as a re-brightening of the afterglow with a typically redder spectrum. Interestingly, the density ring in the wind profile lies closer to the progenitor for WR stars with low initial mass and low metallicity. This characteristic offers a direct observational test of which stars are likely to produce a GRB.

The total energy observed in γ -rays from GRBs whose redshift has been determined is diverse. One appealing aspect of a massive star progenitor is that the great variety of stellar parameters can probably explain this diversity. Given the need for a large helium core mass in progenitors, burst formation may be favoured not only by rapid rotation but also by low metallicity. Larger-mass helium cores might have more energetic jets, but it is unclear whether they can be expected to be accelerated to large Lorentz factors. Many massive stars may produce supernovae by forming neutron stars in spherically symmetric explosions, but some may fail neutrino energy deposition, forming a black hole in the centre of the star and possibly a GRB. One expects various outcomes, ranging from GRBs with large energies and durations to asymmetric energetic supernovae with weak GRBs. The medium surrounding a GRB would provide a natural test to distinguish between different stellar explosions.

ACKNOWLEDGMENTS

We thank P. Natarajan, A. Celotti, G. Morris, G. Koenigsberger, A. MacFadyen and anonymous referee(s) for useful comments and suggestions. We are particularly grateful to A. Blain, R. Chevalier, D. Lazzati, M. Rees and R. Wijers for helpful conversations. ER-R acknowledges support from CONACYT, SEP and the ORS foundation. LMD acknowledges support from PPARC.

REFERENCES

- Abbott D., Conti P., 1987, *ARA&A*, 25, 113
- Akerlof C. W. et al., 1999, *Nat*, 398, 400
- Amati L. et al., 2000, *Sci*, 290, 953
- Blandford R. D., McKee C. F., 1976, *Phys. Fluids*, 19, 1130, (BM)
- Bloom J. S. et al., 1999, *Nat*, 401, 453
- Castor J., Weaver R., McCray R., 1975, *ApJ*, 200, L107
- Castro-Tirado A. J. et al., 1999, *Sci*, 283, 5410, 2069

- Chevalier R. A., Li Z.-Y., 1999, *ApJ*, 520, L29
 Chevalier R. A., Li Z.-Y., 2000, *ApJ*, 536, 195
 Chiosi C., Maeder A., 1986, *ARA&A*, 24, 329
 Cox D. P., 1972, *ApJ*, 178, 159
 de Jager C., Nieuwenhuijzen H., van der Hucht K., 1988, *A&AS*, 72, 259
 Eggleton P. P., 1971, *MNRAS*, 151, 351
 Fenimore E. E., Madras C. D., Nayakshin S., 1996, *ApJ*, 473, 998
 Fenimore E. E., Ramirez-Ruiz E., 2001, *ApJ*, in press (astro-ph/9909299)
 Galama T. J. et al., 1998, *Nat*, 395, 670
 Granot J., Piran T., Sari R., 1998, *ApJ*, 513, 679
 Harries T. J., Hillier D. J., Howarth I. D., 1998, *MNRAS*, 296, 1072
 Harrison F. A. et al., 1999, *ApJ*, 523, L121
 Heger A., Langer N., Woosley S. E., 2000, 528, 368
 Kobayashi S., Piran T., Sari R., 1997, *ApJ*, 490, 92
 Koenigsberger G., 1990, *Rev. Mex. Astron. Astrof.*, 20, 85
 Kulkarni S. R. et al., 1999, *Nat*, 398, 389
 Kumar P., Panaitescu A., 2000, *ApJ*, 541, L9
 Kumar P., Piran T., 2000, *ApJ*, 532, 286
 Kwok S., Purton C. R., Fitzgerald P. M., 1978, *ApJ*, 219, L125
 Langer N., 1987, *A&A*, 171, L1
 Langer N., 1989, *A&A*, 220, 135
 Lattimer J. M., Schramm D. N., 1976, *ApJ*, 210, 549
 Lazzati D., Campana S., Ghisellini G., 1999, *MNRAS*, 304, L31
 Lazzati D. et al., 2001, *A&AM*, submitted
 Luo D., McCray R., 1991, *ApJ*, 379, 659
 MacFadyen A. I., Woosley S. E., 1999, *ApJ*, 524, 262, (MW99)
 MacFadyen A. I., Woosley S. E., Heger A., 1999, *ApJ*, 550, 410
 Madau P., Blandford R. D., Rees M. J., 2000, *ApJ*, 541, 712
 Maeder A., 1991, *A&A*, 242, 93
 Maeder A., Meynet G., 1987, *A&A*, 182, 243
 Maeder A., Meynet G., 2000, *ARA&A*, 38, 143
 Massey P., 1980, *ApJ*, 236, 526
 Massey P., Conti P. S., 1981, *ApJ*, 244, 173
 McCray R., 1983, *Proc. 18th IAU General Assembly, Highlights of Astronomy*, Vol. 6. Reidel, Dordrecht, p. 565
 Mészáros P., Rees M. J., 1997, *ApJ*, 476, 232
 Mészáros P., Rees M. J., 1998, *MNRAS*, 299, L10
 Mészáros P., Rees M. J., Wijers R., 1998, *ApJ*, 499, 301
 Meynet G., Maeder A., Schaller G., Schaerer D., Charbonnel C., 1994, *A&AS*, 103, 97
 Paczyński B., 1998, *ApJ*, 494, L45
 Panaitescu A., Kumar P., 2000, *ApJ*, 543, 66
 Panaitescu A., Mészáros P., Rees M. J., 1998, *ApJ*, 503, 314
 Pian E. et al., 2000, *ApJ*, 536, 778
 Piro L. et al., 1999, *ApJ*, 514, L73
 Piro L. et al., 2000, *Sci*, 290, 955
 Pols O. R., Tout C. A., Eggleton P. P., Han Z., 1995, *MNRAS*, 274, 964
 Ramirez-Ruiz E., Fenimore E. E., 2000, *ApJ*, 539, 712
 Rees M. J., 1999, *A&AS*, 138, 491
 Rees M. J., Mészáros P., 1992, *MNRAS*, 258, L41
 Rees M. J., Mészáros P., 1994, *ApJ*, 430, L93
 Reichart D. E., 1999, *ApJ*, 521, L111
 Rhoads J. E., 1997, *ApJ*, 478, L1
 Sanders D. B., Scoville N. Z., Solomon P. M., 1985, *ApJ*, 289, 373
 Sari R., Piran T., 1995, *ApJ*, 455, L143
 Sari R., Piran T., 1999, *ApJ*, 517, L109
 Sari R., Piran T., Narajan R., 1996, *ApJ*, 473, 218
 Sari R., Piran T., Narajan R., 1998, *ApJ*, 497, L17
 Schröder K. P., Pols O. R., Eggleton P. P., 1997, *MNRAS*, 285, 696
 Shull J. M., 1982, *Regions of Recent Star Formation*. Reidel, Dordrecht, pp. 91–105
 Smith L. F., Hummer D. G., 1988, *MNRAS*, 230, 511
 Smith L. F., Maeder A., 1991, *A&A*, 241, 77
 Vikram D., Balick B., 1998, *ApJ*, 497, 267
 Weth C., Mészáros P., Kallman T., Rees M. J., 2000, *ApJ*, 534, 581
 Woltjer L., 1972, *ARA&A*, 10, 129
 Yoshida A. et al., 1999, *A&AS*, 138, 439

This paper has been typeset from a \LaTeX file prepared by the author.